Chidlow, S and Teodorescu, M

Sliding contact problems involving inhomogeneous materials comprising a coating-transition layer-substrate and a rigid punch

Chidlow, S and Teodorescu, M (2014) Sliding contact problems involving inhomogeneous materials comprising a coating-transition layer-substrate and a rigid punch. *International Journal of Solids and Structures*, 51 (10). pp. 1931-1945.

doi: 10.1016/j.ijsolstr.2014.02.003

# Sliding contact problems involving inhomogeneous materials comprising a coating-transition layer-substrate and a rigid punch

S. J. Chidlow$^{*1}$, M. Teodorescu$^{\dagger}$

$^{*}$*Department of Mechanical Engineering and Mathematical Sciences, Oxford Brookes University, Oxford OX33 1HX, UK*

$^{\dagger}$*Baskin School of Engineering, University of California Santa Cruz 95064, CA USA*

## Abstract

This paper is concerned with a two-dimensional analysis of the contact problem involving a multi-layered elastic solid and a rigid punch. The solid is comprised of a homogeneous coating and substrate joined together by a graded elastic transition layer whose material properties exhibit an exponential dependence on the vertical coordinate. By applying the Fourier Transform to the governing boundary value problem, we formulate expressions for the stresses and displacements induced by the application of point forces acting both normally and tangentially at the origin. The superposition principle is then used to generalise these expressions to the case of distributed normal and tangential tractions acting on the solid surface. A pair of coupled integral equations are further derived for the parabolic stamp problem which are easily solved using collocation methods.

The primary aim of this paper is to provide insight into the likely behaviour of graded materials under pressure. To this end, the assumption of Coulomb friction is invoked within this work and the effects of different coating/interlayer thickness, material gradation and friction coefficient upon the contact footprint and sub-surface stress field are investigated in great detail. The results we obtain

---

[1] *Corresponding author's email address : sj.chidlow@brookes.ac.uk*

suggest that the thickness of the transition layer as well as the combined thickness of the coating and transition layer have a significant effect on the maximum sub-surface stress attained through contact. This indicates that small changes in the composition of the coating can lead to significant differences in material behaviour. We additionally find that an increase in the amount of friction present in the contact can cause dramatic changes in the pattern of the stress field and can give rise to a much larger maximum stress.

## 1. Introduction

Contact problems involving functionally graded materials (FGMs) have received much attention in recent times as such materials are widely used as protective coatings in load transfer problems, typically involving friction. In particular, the gradual variation in material properties helps alleviate some of the problems associated with perfectly bonded, homogeneous layers such as cracking. The potential benefits of using functionally graded materials in such applications are covered in more detail in Suresh (2001) and Suresh et al. (1999).

The majority of proposed models that seek to describe the solution of the contact problem involving FGMs assume that the material is in a state of plane strain and are thus two-dimensional. Ma and Korsunsky (2004) and independently Çömez and Erdöl (2012) model the coating-substrate system as two distinct yet homogeneous perfectly bonded layers. Both authors applied the Fourier transform to the governing two-dimensional boundary value problem (BVP) to derive a pair of singular integral equations from which the normal and tangential pressures resulting from contact by a rigid punch can be determined. In both cases, the tangential pressure resulting from contact is assumed to be a multiple of the normal pressure (Coulomb friction) although their models are not restricted to this assumption. An alternate model was derived by Teodorescu et al. (2009) who proposed an iterative algorithm to determine the contact footprint resulting from the parabolic stamp problem. The authors allowed only for frictionless contact and concentrated on determining the effects of different coatings on the induced sub-surface stress field.

A better assumption that can be used to model functionally graded materials is that the shear modulus of the coating depends on the coordinate system in some way and therefore varies continuously throughout its thickness. Guler and Erdogan (2004) assumed that the shear modulus of the protective coating depends exponentially on the vertical coordinate and using a similar method to that of Ma and Korsunsky determined a coupled pair of singular integral equations from which the normal and tangential tractions caused by contact could be determined. The authors used the assumption of Coulomb friction to produce a series of benchmark solutions for the flat and triangular stamp problems which were further augmented by results presented for the parabolic stamp problem in Guler and Erdogan (2007). Ke and Wang (2006) and Ke and Wang (2007) derived a multi-layer model to determine the solution of the contact problem. The coating was assumed to comprise a series of layers whose shear moduli vary in a piecewise linear fashion which allowed arbitrary shear modulus variations to be considered. The authors compare results produced from their model with those of Guler and Erdogan and both show excellent agreement with each other.

A more complicated model still was proposed by Yang and Ke (2008) who assumed that both the protective coating and substrate are homogeneous but separated by a functionally graded transitional layer comprising an arbitrary number of piecewise linear sub-layers where the properties of the material gradually change from those of the coating to the substrate. The authors consider the rigid parabolic stamp problem and present a series of results indicating how the contact pressure and interfacial stresses are affected by different materials. Choi (2012) used a similar assumption to derive a model to approximate the mode III stress intensity factors that result from two offset interfacial cracks in bonded dissimilar media except that the shear modulus in the interlayer is taken to possess an exponential variation. This approach was also taken by Teixeira (2001) who proposed a numerical model to investigate the influence of a graded layer on the thermal stress distribution within a solid comprising a ceramic coating and a metallic substrate. This work concluded that interlayer thickness has a significant effect on the stress distribution as the optimum condition for stress elimination in a hard coating is obtained when the interlayer is much thicker than the coating.

This paper is concerned with the derivation of a model that approximates the contact footprint and sub-surface stress field within an inhomogeneously elastic solid comprising a homogeneous coating and substrate joined together by a functionally graded transition layer. The proposed model incorporates friction within the contact and provides a natural extension to the type of problem considered by Yang and Ke (2008) and Chidlow and Teodorescu (2013).

The numerical results presented within this work focus on determining the effects of material properties and friction on the sub-surface stress field. King and O'Sullivan (1987) have provided a detailed analysis of this kind for the contact problem involving a layered elastic half space incorporating two distinct homogeneous layers. Their model however does not allow for graded materials and so an attempt is made here to investigate how the presence of the transition layer changes material response. The results presented here detail how changes in material stiffness, coating/interlayer thickness and friction all effect the induced stress field and give implications for potential material failure.

## 2. Fundamental solution of the half-plane problem

Consider an inhomogeneously elastic solid in a state of plane strain occupying the half-plane $y \leq 0$ comprising two finitely thick layers bonded to an infinitely deep substrate (region 3). The upper layer (region 1) occupying $-h_1 \leq y \leq 0$ represents a homogeneously elastic coating whilst the middle layer occupying the region $-h_2 \leq y < -h_1$ represents a graded elastic transition layer (interlayer) where the material properties of the solid progressively change from those of the coating to those of the substrate. The shear modulus of the solid is defined to be

$$\mu(y) = \begin{cases} \mu_1, & -h_1 \leq y \leq 0, \\ \mu_0 e^{\alpha(y+h_2)}, & -h_2 \leq y < -h_1, \\ \mu_0, & -\infty < y < -h_2 \end{cases} \tag{1}$$

where

$$\alpha = \frac{1}{h_2 - h_1} \ln\left(\frac{\mu_1}{\mu_0}\right) \tag{2}$$

which ensures that the shear modulus is continuous everywhere. The Poisson ratio of the solid is assumed constant and is denoted $\nu$.

We introduce the local Airy stress function $\phi_j(x,y)$, $j = 1,2,3$ within each region to determine the stresses induced by pressure applied to the solid surface. The stresses within each region can be calculated from the stress function via the relations

$$\sigma_{yy}^{(j)} = \frac{\partial^2 \phi_j}{\partial x^2}, \qquad \sigma_{xx}^{(j)} = \frac{\partial^2 \phi_j}{\partial y^2}, \qquad \sigma_{xy}^{(j)} = -\frac{\partial^2 \phi_j}{\partial x \partial y}. \tag{3}$$

Substituting (1) into the compatibility condition valid for a two-dimensional material (see Timoshenko and Goodier (1970) for example) reveals that the local stress functions satisfy

$$\nabla^4 \phi_1 = 0, \tag{4}$$

$$\nabla^4 \phi_2 - 2\alpha \frac{\partial}{\partial y}\left(\nabla^2 \phi_2\right) + \alpha^2 \frac{\partial^2 \phi_2}{\partial y^2} - \alpha^2 \rho \frac{\partial^2 \phi_2}{\partial x^2} = 0, \tag{5}$$

$$\nabla^4 \phi_3 = 0 \tag{6}$$

with

$$\nabla^2 = \frac{\partial^2}{\partial x^2} + \frac{\partial}{\partial y^2}$$

denoting the Laplacian operator and $\rho = \nu/(1-\nu)$. We may apply the Fourier transform which we define as

$$\tilde{\phi}_j(\xi, y) = \int_{-\infty}^{\infty} \phi_j(x, y) e^{i\xi x} \mathrm{d}x \tag{7}$$

to (4)-(6) which results in the transformed equations

$$\tilde{\phi}_1'''' - 2\xi^2 \tilde{\phi}_1'' + \xi^4 \tilde{\phi}_1 = 0, \tag{8}$$

$$\tilde{\phi}_2'''' - 2\alpha \tilde{\phi}_2''' + \left(\alpha^2 - 2\xi^2\right) \tilde{\phi}_2'' + 2\alpha \xi^2 \tilde{\phi}_2' + \xi^2 \left(\xi^2 + \rho \alpha^2\right) \tilde{\phi}_2 = 0, \tag{9}$$

$$\tilde{\phi}_3'''' - 2\xi^2 \tilde{\phi}_3'' + \xi^4 \tilde{\phi}_3 = 0 \tag{10}$$

where $'$ denotes differentiation with respect to $y$. Equations (8)-(10) admit the general solutions

$$\tilde{\phi}_1(\xi, y) = (C_1 + C_2 y)\, e^{|\xi| y} + (C_3 + C_4 y)\, e^{-|\xi| y}, \tag{11}$$

$$\tilde{\phi}_2(\xi, y) = \sum_{n=1}^{4} A_n e^{\lambda_n y}, \tag{12}$$

$$\tilde{\phi}_3(\xi, y) = (D_1 + D_2 y)\, e^{|\xi| y} + (D_3 + D_4 y)\, e^{-|\xi| y} \tag{13}$$

where the roots $\lambda_n$ satisfy the quartic equation

$$\lambda^4 - 2\alpha\lambda^3 + \left(\alpha^2 - 2\xi^2\right)\lambda^2 + 2\alpha\xi^2\lambda + \xi^2\left(\xi^2 + \rho\alpha^2\right) = 0 \tag{14}$$

and may be written explicitly as

$$\lambda_1 = \sqrt{\frac{1}{4}(\alpha^2 + 4\xi^2) + i\alpha|\xi|\sqrt{\rho}} + \frac{1}{2}\alpha, \tag{15a}$$

$$\lambda_2 = -\sqrt{\frac{1}{4}(\alpha^2 + 4\xi^2) + i\alpha|\xi|\sqrt{\rho}} + \frac{1}{2}\alpha, \tag{15b}$$

$$\lambda_3 = \sqrt{\frac{1}{4}(\alpha^2 + 4\xi^2) - i\alpha|\xi|\sqrt{\rho}} + \frac{1}{2}\alpha, \tag{15c}$$

$$\lambda_4 = -\sqrt{\frac{1}{4}(\alpha^2 + 4\xi^2) - i\alpha|\xi|\sqrt{\rho}} + \frac{1}{2}\alpha. \tag{15d}$$

The constants appearing in the solution above are $\xi$-dependent and are obtained by specifying boundary conditions for this problem. We assume here that the transition layer is perfectly bonded to both the coating and substrate and thus enforce the continuity of both the stresses and displacements across each interface. Mathematically we stipulate that

$$\begin{aligned} u^{(i)} &= u^{(i+1)}, \\ v^{(i)} &= v^{(i+1)}, \\ \sigma_{yy}^{(i)} &= \sigma_{yy}^{(i+1)}, \\ \sigma_{xy}^{(i)} &= \sigma_{xy}^{(i+1)} \end{aligned} \tag{16}$$

at $y = -h_i$, $i = 1, 2$ where $u^{(j)}(x,y)$ and $v^{(j)}(x,y)$ denote the horizontal and vertical displacement of the solid in the $j$th region respectively. We further require that the induced stresses and displacements vanish as $y \to -\infty$ and thus we impose the radiation conditions $|u|, |v| \to 0$ as $y \to -\infty$. The

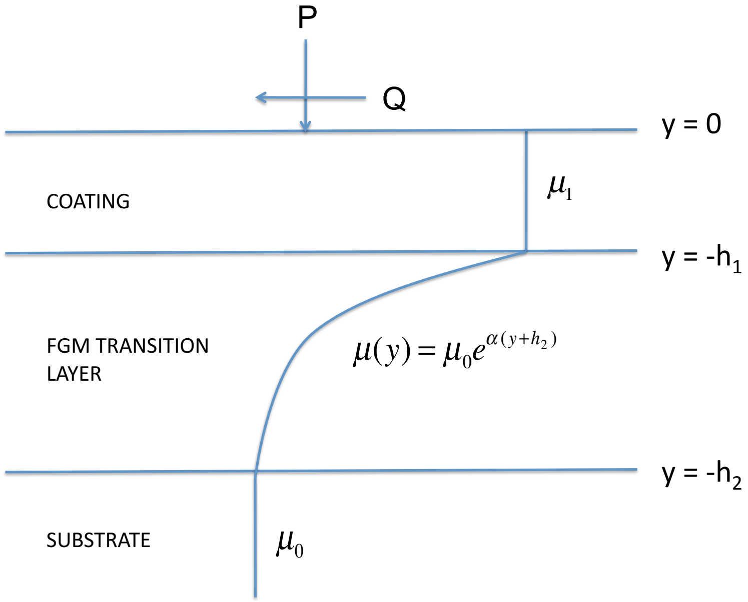

Figure 1: A definition sketch of the point force problem investigated in Section 2.

remaining boundary conditions are applied on the solid surface ($y = 0$) and specify that

$$\sigma_{yy} = -P(x), \tag{17}$$

$$\sigma_{xy} = -Q(x). \tag{18}$$

We initially consider the state of stress that results in the solid from the application of point forces to its surface so we take $P(x) = \delta(x)P$, $Q(x) = \delta(x)Q$ where $\delta(x)$ denotes the Dirac delta function centred at the origin (see figure (1)). A discussion of how these solutions may be generalised to distributed normal and tangential tractions is provided in the next section.

It is easily observed that the radiation conditions applied as $y \to -\infty$ imply that $D_3 = D_4 = 0$. Applying the Fourier transform to the remaining boundary and matching conditions allows us to deduce that the constants appearing in (11) possess the closed form solutions

$$\begin{pmatrix} C_1 \\ \\ C_2 \end{pmatrix} = \Phi^{-1} \begin{pmatrix} \frac{P}{\xi^2} \\ \\ \frac{iQ}{\xi} \end{pmatrix}, \tag{19}$$

$$\begin{pmatrix} C_3 \\ \\ C_4 \end{pmatrix} = -e^{-2|\xi|h_1} \left(J_1 - SW^{-1}L_1\right)^{-1} \left(H_1 - SW^{-1}G_1\right) \Phi^{-1} \begin{pmatrix} \frac{P}{\xi^2} \\ \\ \frac{iQ}{\xi} \end{pmatrix} \tag{20}$$

whilst the remaining constants can be computed from the relations

$$\begin{pmatrix} A_1 \\ \\ A_3 \end{pmatrix} = W^{-1} \left( e^{-|\xi|h_1} G_1 \begin{pmatrix} C_1 \\ \\ C_2 \end{pmatrix} + e^{|\xi|h_1} L_1 \begin{pmatrix} C_3 \\ \\ C_4 \end{pmatrix} \right), \tag{21}$$

$$\begin{pmatrix} A_2 \\ \\ A_4 \end{pmatrix} = -(T_2 K_2^{(2)})^{-1} T_1 K_1^{(2)} \begin{pmatrix} A_1 \\ \\ A_3 \end{pmatrix}, \tag{22}$$

$$\begin{pmatrix} D_1 \\ \\ D_2 \end{pmatrix} = e^{|\xi|h_2} G_2^{-1} \left( M_1 K_1^{(2)} \begin{pmatrix} A_1 \\ \\ A_3 \end{pmatrix} + M_2 K_2^{(2)} \begin{pmatrix} A_2 \\ \\ A_4 \end{pmatrix} \right). \tag{23}$$

Please see Appendix A for the definition of the matrices appearing in (19)-(23).

The stresses induced within the solid and its displacement at any point may now be computed by applying the inverse Fourier transform. In particular, we note that the horizontal and vertical displacement of the solid surface may be written as

$$\begin{pmatrix} u(x,0) \\ \\ v(x,0) \end{pmatrix} = \frac{1}{4\pi\mu_1} \int_{-\infty}^{\infty} \Theta(\xi) Z(\xi) (P,Q)^T e^{-i\xi x} \mathrm{d}\xi, \tag{24}$$

where

$$\Theta(\xi) = \begin{pmatrix} i\xi & 2i(1-\nu)\mathrm{sign}(\xi) & i\xi & -2i(1-\nu)\mathrm{sign}(\xi) \\ -|\xi| & (1-2\nu) & |\xi| & (1-2\nu) \end{pmatrix}, \tag{25}$$

$$Z(\xi) = \begin{pmatrix} \chi \\ \Psi \end{pmatrix}, \tag{26}$$

$$\chi(\xi) = \Phi^{-1} \begin{pmatrix} \frac{1}{\xi^2} & 0 \\ 0 & \frac{i}{\xi} \end{pmatrix}, \tag{27}$$

$$\Psi(\xi) = -e^{-2|\xi|h_1} \left(J_1 - SW^{-1}L_1\right)^{-1} \left(H_1 - SW^{-1}G_1\right) \chi. \tag{28}$$

We note that the entries of the matrices $\Theta$ and $Z$ satisfy

$$\Theta_{ij}(-\xi) = (-1)^{i+j}\Theta_{ij}(\xi), \tag{29}$$

$$Z_{i1}(-\xi) = Z_{i1}(\xi), \tag{30}$$

$$Z_{i2}(-\xi) = -Z_{i2}(\xi) \tag{31}$$

for $i, j = 1,2$ and so the displacements appearing in (24) can be written in the alternate form

$$\begin{aligned} u_1(x,0) = \frac{1}{2\pi\mu_1}\Bigg( & P\int_0^\infty \left(\xi(\chi_{11}+\Psi_{11}) + 2(1-\nu)(\chi_{21}-\Psi_{21})\right)\sin(\xi x)\mathrm{d}\xi \\ & + iQ\int_0^\infty \left(\xi(\chi_{12}+\Psi_{12}) + 2(1-\nu)(\chi_{22}-\Psi_{22})\right)\cos(\xi x)\mathrm{d}\xi\Bigg), \end{aligned} \tag{32}$$

$$\begin{aligned} v_1(x,0) = \frac{1}{2\pi\mu_1}\Bigg( & P\int_0^\infty \left((1-2\nu)(\chi_{21}+\Psi_{21}) - \xi(\chi_{11}-\Psi_{11})\right)\cos(\xi x)\mathrm{d}\xi \\ & + iQ\int_0^\infty \left(\xi(\chi_{12}-\Psi_{12}) - (1-2\nu)(\chi_{22}+\Psi_{22})\right)\sin(\xi x)\mathrm{d}\xi\Bigg). \end{aligned} \tag{33}$$

Equations (32) and (33) are not ideal to work with in this form as the integrals appearing within these formulae need to be evaluated numerically but are not obviously convergent. We can remedy this problem however by considering the behaviour of the the constants $C_j$, $j = 1,...,4$ as $\xi \to \infty$. In this limit, the constants $C_j$ reduce to

$$\begin{pmatrix} C_1 \\ \\ C_2 \end{pmatrix} \to H_0^{-1} \begin{pmatrix} \frac{P}{\xi^2} \\ \\ \frac{iQ}{\xi} \end{pmatrix}, \tag{34}$$

$$\begin{pmatrix} C_3 \\ \\ C_4 \end{pmatrix} \to 0 \tag{35}$$

and so

$$\begin{pmatrix} \tilde{u}(\xi,0) \\ \\ \tilde{v}(\xi,0) \end{pmatrix} \to \begin{pmatrix} \hat{f}(\xi) \\ \\ \hat{g}(\xi) \end{pmatrix} = -\frac{1}{2\mu_1\xi} \begin{pmatrix} i(1-2\nu)P + 2(1-\nu)\mathrm{sign}(\xi)Q \\ \\ 2(1-\nu)\mathrm{sign}(\xi)P - i(1-2\nu)Q \end{pmatrix} \tag{36}$$

as $\xi \to \infty$. Applying the inverse Fourier transform to these functions then gives

$$\begin{aligned} f(x) &= -\frac{1}{4\pi\mu_1}\int_{-\infty}^{\infty}\left(\frac{i(1-2\nu)P}{\xi} + \frac{2(1-\nu)\mathrm{sign}(\xi)Q}{\xi}\right)e^{-i\xi x}\mathrm{d}\xi, \\ &= -\frac{1}{2\pi\mu_1}\left(\frac{\pi}{2}P(1-2\nu)\mathrm{sign}(x) - 2(1-\nu)Q\ln|x|\right), \end{aligned} \tag{37}$$

$$\begin{aligned} g(x) &= -\frac{1}{4\pi\mu_1}\int_{-\infty}^{\infty}\left(\frac{2(1-\nu)\mathrm{sign}(\xi)P}{\xi} - \frac{i(1-2\nu)Q}{\xi}\right)e^{-i\xi x}\mathrm{d}\xi \\ &= \frac{1}{2\pi\mu_1}\left(2(1-\nu)\ln|x|P + \frac{\pi}{2}(1-2\nu)\mathrm{sign}(x)Q\right) \end{aligned} \tag{38}$$

which follow from the standard results

$$\int_0^\infty \frac{\cos(\xi x)}{\xi}\mathrm{d}\xi = -\ln|x|, \tag{39}$$

$$\int_0^\infty \frac{\sin(\xi x)}{\xi}\mathrm{d}\xi = \frac{\pi}{2}\mathrm{sign}(x). \tag{40}$$

By adding the integrated forms of (37) and (38) to (32) and (33) and subtracting their corresponding integral forms, we may write

$$
\begin{aligned}
u_1(x,0) = &-\frac{(1-2\nu)\mathrm{sign}(x)P}{4\mu_1} + \frac{(1-\nu)\ln|x|Q}{\pi\mu_1} \\
&+ \frac{1}{2\pi\mu_1}\left(P\int_0^\infty \left(\xi(\chi_{11}+\Psi_{11}) + 2(1-\nu)(\chi_{21}-\Psi_{21}) + \frac{(1-2\nu)}{\xi}\right)\sin(\xi x)\mathrm{d}\xi\right. \\
&\left.+ iQ\int_0^\infty \left(\xi(\chi_{12}+\Psi_{12}) + 2(1-\nu)(\chi_{22}-\Psi_{22}) - \frac{2i(1-\nu)}{\xi}\right)\cos(\xi x)\mathrm{d}\xi\right), \qquad (41)\\
v_1(x,0) = &\frac{(1-\nu)\ln|x|}{\pi\mu_1}P + \frac{(1-2\nu)\mathrm{sign}(x)}{4\mu_1} \\
&+ \frac{1}{2\pi\mu_1}\left(P\int_0^\infty \left((1-2\nu)(\chi_{21}+\Psi_{21}) - \xi(\chi_{11}-\Psi_{11}) + \frac{2(1-\nu)}{\xi}\right)\cos(\xi x)\mathrm{d}\xi\right. \\
&\left.+ iQ\int_0^\infty \left(\xi(\chi_{12}-\Psi_{12}) - (1-2\nu)(\chi_{22}+\Psi_{22}) + \frac{i(1-2\nu)}{\xi}\right)\sin(\xi x)\mathrm{d}\xi\right). \qquad (42)
\end{aligned}
$$

We note immediately that the integrals appearing in (41) and (42) are convergent as the integrands tend to zero as $\xi \to \infty$ and thus these integrals can be easily evaluated numerically. These terms inform the effects of material inhomogeneity on the surface displacement whilst the non-integral terms correspond to the horizontal and vertical displacements of the solid surface of a homogeneous material (see Johnson (1985)).

## 3. Contact problems involving a rigid punch

The solutions derived in the previous section for the case of point forces applied at the origin can be generalised to solve the rigid punch problem. A definition sketch of this problem is presented in figure (2). In this situation, contact will occur between the punch and solid surface in some interval $[-b,a]$ with the result that both the normal and tangential pressures applied to the solid will be non-zero only within this interval. We refer to the normal pressure as $p(x)$ and friction force as $q(x)$ within this section.

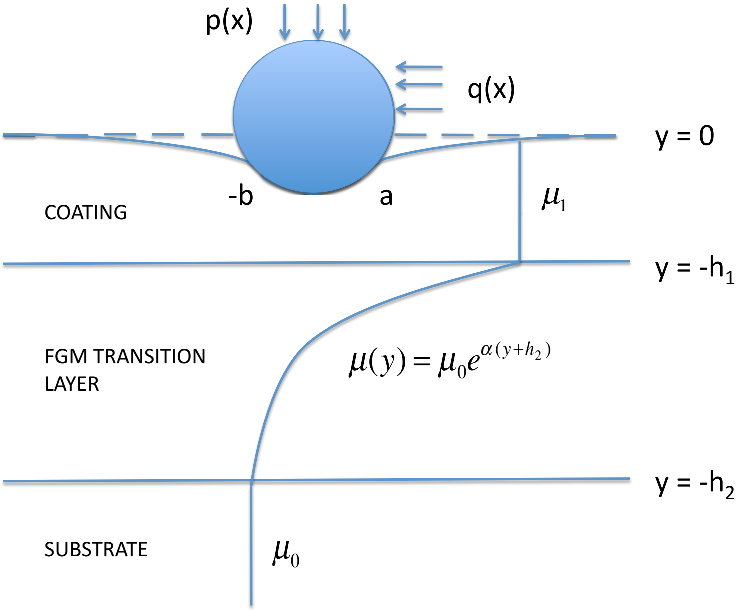

Figure 2: A definition sketch of the parabolic punch problem investigated in Section 3.

Applying the superposition principle to (41) and (42) gives the displacement of the solid surface as

$$\begin{aligned} u_1(x,0) &= -\frac{(1-2\nu)}{4\mu_1}\int_{-b}^{a}\operatorname{sign}(x-t)p(t)\mathrm{d}t+\frac{(1-\nu)}{\pi\mu_1}\int_{-b}^{a}\ln|x-t|q(t)\mathrm{d}t \\ &\quad+\frac{1}{2\pi\mu_1}\int_{-b}^{a}L_1(x,t)p(t)\mathrm{d}t+\frac{i}{2\pi\mu_1}\int_{-b}^{a}L_2(x,t)q(t)\mathrm{d}t, \qquad (43) \end{aligned}$$

$$\begin{aligned} v_1(x,0) &= \frac{(1-\nu)}{\pi\mu_1}\int_{-b}^{a}\ln|x-t|p(t)\mathrm{d}t+\frac{(1-2\nu)}{4\mu_1}\int_{-b}^{a}\operatorname{sign}(x-t)q(t)\mathrm{d}t \\ &\quad+\frac{1}{2\pi\mu_1}\int_{-b}^{a}L_3(x,t)p(t)\mathrm{d}t+\frac{i}{2\pi\mu_1}\int_{-b}^{a}L_4(x,t)q(t)\mathrm{d}t \qquad (44) \end{aligned}$$

where

$$L_1(x,t)=\int_0^\infty\left(\xi(\chi_{11}+\Psi_{11})+2(1-\nu)(\chi_{21}-\Psi_{21})+\frac{(1-2\nu)}{\xi}\right)\sin(\xi(x-t))\mathrm{d}\xi, \tag{45}$$

$$L_2(x,t)=\int_0^\infty\left(\xi(\chi_{12}+\Psi_{12})+2(1-\nu)(\chi_{22}-\Psi_{22})-\frac{2i(1-\nu)}{\xi}\right)\cos(\xi(x-t))\mathrm{d}\xi, \tag{46}$$

$$L_3(x,t)=\int_0^\infty\left(-\xi(\chi_{11}-\Psi_{11})+(1-2\nu)(\chi_{21}+\Psi_{21})+\frac{2(1-\nu)}{\xi}\right)\cos(\xi(x-t))\mathrm{d}\xi, \tag{47}$$

$$L_4(x,t)=\int_0^\infty\left(\xi(\chi_{12}-\Psi_{12})-(1-2\nu)(\chi_{22}+\Psi_{22})+\frac{i(1-2\nu)}{\xi}\right)\sin(\xi(x-t))\mathrm{d}\xi. \tag{48}$$

In the rigid punch problem, the gradient of the surface deflection will be known rather than the deflection itself as the punch profile will be given. We therefore differentiate (43) and (44) with respect to $x$ to obtain

$$\begin{aligned}\frac{\partial u_1}{\partial x}(x,0)=&-\frac{(1-2\nu)}{2\mu_1}p(x)-\frac{(1-\nu)}{\pi\mu_1}\int_{-b}^{a}\frac{q(t)}{t-x}\mathrm{d}t\\&+\frac{1}{2\pi\mu_1}\int_{-b}^{a}\frac{\partial L_1}{\partial x}(x,t)p(t)\mathrm{d}t+\frac{i}{2\pi\mu_1}\int_{-b}^{a}\frac{\partial L_2}{\partial x}(x,t)q(t)\mathrm{d}t \qquad (49)\\\frac{\partial v_1}{\partial x}(x,0)=&\frac{(1-2\nu)}{2\mu_1}q(x)-\frac{(1-\nu)}{\pi\mu_1}\int_{-b}^{a}\frac{p(t)}{t-x}\mathrm{d}t\\&+\frac{1}{2\pi\mu_1}\int_{-b}^{a}\frac{\partial L_3}{\partial x}(x,t)p(t)\mathrm{d}t+\frac{i}{2\pi\mu_1}\int_{-b}^{a}\frac{\partial L_4}{\partial x}(x,t)q(t)\mathrm{d}t. \qquad (50)\end{aligned}$$

Equations (49) and (50) constitute a pair of coupled integral equations which may be solved for the unknown functions $p(x)$ and $q(x)$ provided that we know the stamp profile and contact conditions. It is assumed here for simplicity that friction is of Coulomb type so that

$$q(x)=\eta p(x) \tag{51}$$

and thus we have only one unknown function to determine. Substituting (51) into (50) gives

$$\frac{\eta(1-2\nu)}{2\mu_1}p(x)-\frac{(1-\nu)}{\pi\mu_1}\int_{-b}^{a}\frac{p(t)}{t-x}\mathrm{d}t+\frac{1}{\pi}\int_{-b}^{a}\big(I_3(x,t)+i\eta I_4(x,t)\big)p(t)\mathrm{d}t=g(x) \tag{52}$$

where

$$I_j(x,t) = \frac{1}{2\mu_1}\frac{\partial L_j}{\partial x}, \qquad j = 1,...,4 \tag{53}$$

$$g(x) = \frac{\partial v_1}{\partial x}(x,0), \tag{54}$$

which holds for $-b \leq t,x \leq a$. The uniqueness of the solution $p(x)$ obtained from (52) is assured by enforcing the condition

$$\int_{-b}^{a} p(x)\mathrm{d}x = W \tag{55}$$

which stipulates that the integral of the normal pressure over the contact region is equivalent to the total compressive force.

### *3.1. Approximating the solution of the integral equation*

As (52) is a singular integral equation of the second kind, it may be solved numerically using the collocation method proposed by Krenk (1975). We briefly discuss how this method may be applied here but refer readers to Ke and Wang (2007) for a more detailed discussion.

In order to apply the relevant collocation technique, we need to non-dimensionalise the contact region so that $-b \leq x,t \leq a$ corresponds to $-1 \leq \zeta,\tau \leq 1$. The requisite mappings are

$$x = \frac{1}{2}\Big((b+a)\zeta - (b-a)\Big), \tag{56}$$

$$t = \frac{1}{2}\Big((b+a)\tau - (b-a)\Big) \tag{57}$$

which allow us to write (52) as

$$\frac{\eta(1-2\nu)}{2\mu_1}p(\zeta) - \frac{(1-\nu)}{\pi\mu_1}\int_{-1}^{1}\frac{1}{\tau-\zeta}p(\tau)\mathrm{d}\tau + \frac{(b+a)}{2\pi}\int_{-1}^{1}\Big(I_3(\zeta,\tau)+i\eta I_4(\zeta,\tau)\Big)p(\tau)\mathrm{d}\tau = g(\zeta). \tag{58}$$

We now assume that the pressure can be written in the form

$$p(\zeta) = f(\zeta)(1-\zeta)^{\beta_1}(1-\zeta)^{\beta_2}, \tag{59}$$

where

$$\beta_1 = \frac{1}{\pi}\tan^{-1}\left(\frac{2(1-\nu)}{\eta(1-2\nu)}\right) + N_0, \tag{60}$$

$$\beta_2 = -\frac{1}{\pi}\tan^{-1}\left(\frac{2(1-\nu)}{\eta(1-2\nu)}\right) + M_0 \tag{61}$$

for arbitrary integers $N_0$, $M_0$ which are determined from the physics of the problem. In the case of contact by a parabolic stamp, the collocation method of Krenk (1975) reduces (58) to the system

$$\sum_{i=1}^{M} W_i^M \left(-\frac{(1-\nu)}{\mu_1(\tau_i-\zeta_k)} + \frac{(b+a)}{2}\Big(I_3(\zeta_k,\tau_i) + i\eta(\zeta_k,\tau_i)\Big)\right) f(\tau_i) = g(\zeta_k), \qquad k = 1,\ldots,M+1 \tag{62}$$

where

$$g(\zeta_k) = \frac{(b+a)\zeta_k - (b-a)}{2R} \tag{63}$$

which follows from applying the change of variable to the parabolic stamp profile. The corresponding equilibrium condition (55) is transformed into

$$\sum_{i=1}^{M} W_i^M f(\tau_i) = \frac{2W}{\pi(b+a)}, \tag{64}$$

where the weights $W_i^M$ appearing in these equations are defined as

$$W_i^M = -2^{-(N_0+M_0)}\frac{\Gamma(\beta_1)\Gamma(1-\beta_1)}{\pi} \tag{65}$$

and $\Gamma$ denotes the Gamma function. The collocation points used within this method satisfy

$$P_n^{(\beta_1,\beta_2)}(\tau_i) = 0, \tag{66}$$

$$P_{n+1}^{(-\beta_1,-\beta_2)}(\zeta_k) = 0 \tag{67}$$

for $i = 1,...,M$, $k = 1,...,M+1$ where $P_n^{(\beta_1,\beta_2)}(\tau)$ denotes the Jacobi polynomial of degree $n$. The unknowns that appear within (62) and (64) are the values of the function $f$ at the $M$ specified gridpoints and the values of $a$ and $b$. We therefore have $M+2$ unknowns in $M+2$ equations.

In order to solve the contact problem, we need to compute the values of $a$ and $b$ iteratively. We choose initial guesses for $a$ and $b$ denoted $a_0$ and $b_0$ and solve the first $M$ equations in (62) to determine the values of $f$ at the $M$ designated gridpoints. We use the $(M+1)$th equation in (62) and (64) to update our approximations to $a$ and $b$ using the Secant method. The stopping criteria used in this method is

$$\max\left(b_{n+1}-b_n, a_{n+1}-a_n\right) < 1\times 10^{-8} \tag{68}$$

which ensures that a good degree of accuracy is obtained in the solution.

## 4. Model Validation

In this section, we compare results produced using this model to those of other authors in two different limiting cases. This serves as a check on the accuracy of our model and allows us to validate it before presenting new results for the problem of sliding contact.

### *4.1. Example 1*

We initially attempt to recreate the results of Çömez and Erdöl (2012) who derived a model to approximate the solution of the parabolic stamp problem involving a solid comprising two distinct, homogeneous layers. As we cannot recreate this situation exactly as $\alpha \to \infty$ in this limit, we consider what happens as $h_2 - h_1$ becomes increasingly small.

The parameter values used in this problem are

$$\frac{R}{h_1} = 500, \qquad \frac{\mu_1 h_1}{W} = 50, \qquad \frac{\mu_1}{\mu_0} = 2, \qquad \nu = 0.25$$

whilst we consider two different interlayer thicknesses to see how our model behaves as $h_2 - h_1 \to 0$. The two representative thicknesses chosen satisfy

$$\frac{h_2 - h_1}{h_1} = 0.01, 0.001.$$

The results produced using these values and those of Çömez and Erdöl (2012) are contained in table (1) and indicate good agreement between models. We see that the results produced for the thinner interlayer are closer to those of Çömez and Erdöl (2012) and thus we deduce that in the limit $h_2 - h_1 \to 0$, our model describes a solid comprising a homogeneously elastic coating bonded to a distinct homogeneous substrate as expected.

| | Cömez and Erdöl | | $(h_2 - h_1)/h_1 = 0.01$ | | $(h_2 - h_1)/h_1 = 0.001$ | |
|---|---|---|---|---|---|---|
| $\eta$ | Half-width | Eccentricity | Half-width | Eccentricity | Half-width | Eccentricity |
| 0 (uncoated) | 3.09020 | 0 | 3.09019 | 0 | 3.09019 | 0 |
| 0 | 2.74060 | 0 | 2.73925 | 0 | 2.74045 | 0 |
| 0.4 | 2.75159 | 0.23674 | 2.75028 | 0.23679 | 2.75147 | 0.23675 |
| 0.8 | 2.78367 | 0.47046 | 2.78238 | 0.47054 | 2.78355 | 0.47046 |
| 1 | 2.80682 | 0.58537 | 2.80556 | 0.58545 | 2.80670 | 0.58536 |

Table 1: Variation of the contact-half width and eccentricity with increased friction coefficient. The results produced using our model are compared to those of Çömez and Erdöl (2012).

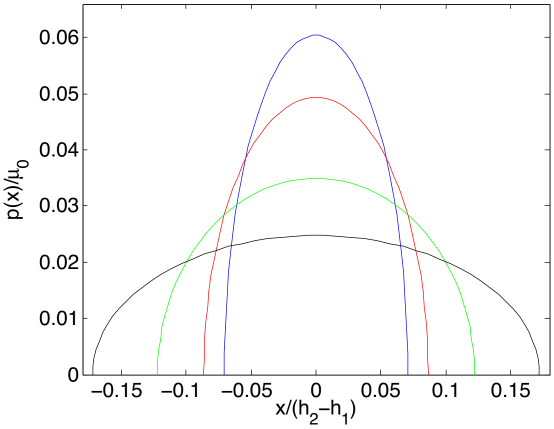

Figure 3: Contact pressure curves produced for the problem originally considered by Yang and Ke (2008). The blue line represents $\mu_1/\mu_0 = 3$, the red line $\mu_1/\mu_0 = 2$, the green line $\mu_1/\mu_0 = 1$ and the black line $\mu_1/\mu_0 = 0.5$.

### *4.2. Example 2*

We now validate our model further by comparing our results with those of Yang and Ke (2008). These authors considered a frictionless contact problem involving a rigid parabolic stamp and solid comprising a coating-graded layer-substrate where the graded layer is split into several sub-layers whose shear moduli have a linear dependence on the vertical coordinate. In the example we consider, these authors used their piecewise linear model to approximate an exponentially varying shear modulus within the transition layer.

The parameter values used within this problem are

$$\frac{h_1}{h_2} = 1, \qquad \nu = 0.3, \qquad \frac{R}{h_2} = 5, \qquad \frac{W}{\mu_0 h_2} = 6.7 \times 10^{-3}$$

whilst the four different coatings satisfying $\mu_1/\mu_0 = 0.5, 1, 2, 3$ are used. The results produced using our model are presented in figure (3) and show excellent agreement with those of Yang and Ke as expected (compare with their figure 5).

## 5. Computing the sub-surface stress field

As we have validated our model against the results of other authors, we can now look to produce results for the full sliding contact problem. In what follows, we will mainly be interested in how different parameters (e.g. coating/interlayer thickness, friction coefficient) effect the sub-surface stress fields that result from contact. Using (3), we may write

$$\sigma_{yy}^{(j)} = -\frac{1}{2\pi}\int_{-\infty}^{\infty} \xi^2 \hat{\phi}_j(\xi,y)e^{-i\xi x}\mathrm{d}\xi, \tag{69}$$

$$\sigma_{xx}^{(j)} = \frac{1}{2\pi}\int_{-\infty}^{\infty} \hat{\phi}_j''(\xi,y)e^{-i\xi x}\mathrm{d}\xi, \tag{70}$$

$$\sigma_{xy}^{(j)} = \frac{i}{2\pi}\int_{-\infty}^{\infty} \xi\hat{\phi}_j'(\xi,y)e^{-i\xi x}\mathrm{d}\xi \tag{71}$$

where $j = 1,2,3$ denotes the different regions within the solid. As the constants that appear in the solutions of $\hat{\phi}_j$ are very complicated in form, the integrals appearing in (69)-(71) cannot be evaluated analytically. Instead, we use the inverse discrete Fourier transform (IDFT) to approximate these quantities. The discretisation used within this work is slightly different from that used in the standard IDFT and is described below.

Let $x$ occupy the finite length interval $[-L,L]$ which is split into $N-1$ sub-intervals of width $\Delta$ and let the frequency variable $\omega = \xi/2\pi$ occupy the finite interval $[-\omega_F,\omega_F]$. We define the $n$th coordinate in the spatial domain and the $k$th value in the frequency domain to be

$$x_n = -L+(n-1)\Delta, \tag{72}$$

$$\omega_k = \frac{1}{2N\Delta}\Big(2(k-1)-(N-1)\Big) \tag{73}$$

for $n,k=1,...,N$. The IDFT of an arbitrary function $\hat{s}(\omega)$ is defined as

$$s(x_n)=\frac{1}{N\Delta}\sum_{k=1}^{N}\hat{s}(\omega_k)e^{-2\pi\imath\omega_k}, \qquad n=1,...,N, \tag{74}$$

which using (72) and (73) can be written as

$$s(x_n)=\frac{e^{\frac{\pi i(N-1)}{N\Delta}\left((n-1)\Delta-L\right)}}{N\Delta}\sum_{k=1}^{N}\hat{s}(\omega_k)e^{\frac{2\pi iL(k-1)}{N\Delta}}e^{-\frac{2\pi i}{N}(k-1)(n-1)}. \tag{75}$$

By denoting

$$S(\omega_k)=\hat{s}(\omega_k)e^{\frac{2\pi iL(k-1)}{N\Delta}}, \tag{76}$$

$$W_N=e^{-\frac{2\pi i}{N}}, \tag{77}$$

we may re-write (75) as

$$s(x_n)=\frac{e^{\frac{\pi i(N-1)}{N\Delta}\left((n-1)\Delta-L\right)}}{N\Delta}\sum_{k=1}^{N}S(\omega_k)W_n^{(k-1)(n-1)}. \tag{78}$$

The IDFT is now in the correct form to evaluate using the fast Fourier transform algorithms (FFT). We choose to use the classical Cooley and Tukey algorithm within this work so $N$ will be taken to be a power of 2.

## 6. Numerical Results

We conclude this work with an investigation into the full three-layer sliding contact problem. As before, we consider contact by a parabolic stamp subject to the fixed parameter values

$$\nu=0.3, \qquad R=5\text{cm}, \qquad W=10000\text{N}, \qquad \frac{h_2}{a_h}=1,$$

with $a_h$ denoting the predicted Hertzian contact half-width. The formulae for this quantity and the maximum predicted Hertzian pressure are included below for brevity. These values are used here to allow us to compare results against those produced for a homogeneous material in the classic contact problem and because it will allow an easy comparison with the results of Chidlow and Teodorescu (2013).

$$a_h = \sqrt{\frac{2WR(1-\nu)}{\pi\mu_1}}, \qquad p_h = \frac{2W}{\pi a_h}. \tag{79}$$

Our aim within this example is to determine how coating and interlayer thickness as well as increasing friction effect the predicted contact footprint and stress field. With this in mind, we begin this example by considering how the predicted contact pressure curves $p(x)$ and contact half-width $H = (a+b)/2$ obtained for a selection of different coatings are affected by different values of the friction coefficient $\eta$ and coating/layer thickness ratio $h_1/h_2$. Please note that in what follows, coatings that satisfy $\frac{\mu_1}{\mu_0} > 1$ are referred to as hard whilst coatings that satisfy $\frac{\mu_1}{\mu_0} < 1$ are called soft.

The predicted contact half-widths and pressure curves produced here are non-dimensionalised using the relevant Hertzian parameters in order to compare our solutions with the classical frictionless punch problem involving a homogeneous material. We therefore define the new quantities

$$\bar{p}(x) = \frac{p(x)}{p_h}, \tag{80}$$

$$\bar{H} = \frac{(b+a)}{2a_h} \tag{81}$$

which represent the dimensionless contact pressure and dimensionless contact half-width respectively.

### *6.1. Predicted contact footprint*

We initially examine the pressure curves produced for five different coatings satisfying $\mu_1/\mu_0 = 0.25, 0.5, 1, 2, 4$ subject to the coating thickness/layer thickness ratio satisfying $h_1/h_2 = 0.1$. The value of $\eta$ is fixed within each problem but is allowed to vary between problems.

The predicted contact pressure curves corresponding to these parameter values are presented in figure (4). This figure indicates that hard coatings experience larger maximum pressures than soft coatings but act over a smaller area. These observations are in accord with those of Chidlow and Teodorescu (2013) and Yang and Ke (2008). We also note that when $\eta = 0$, $b = a$ and so the contact interval is symmetric about the origin. As the friction coefficient increases in value, we see that $b < a$ so the contact interval and pressure curve becomes skewed about the origin. This has the additional effect that the maximum pressure occurs to the right of the origin rather than at the origin.

We may more fully examine how the contact pressure, and in particular, the location at which its maximum occurs is affected by friction by examining how different values of $\eta$ affect one particular coating. The results depicted in figure (5) show the contact pressure curves produced for the hard coating satisfying $\mu_1/\mu_0 = 2$ and the soft coating satisfying $\mu_1/\mu_0 = 0.5$ of thickness $h_1/h_2 = 0.1, 0.9$ subject to the friction coefficients $\eta = 0, 0.1, 0.2, 0.3, 0.4$. It is clearly visible here that the value of $\eta$ does affect both the location of the maximum pressure and how much the contact interval moves from left to right. We note however that the value of the maximum pressure and the width of the contact interval are completely unaffected by any increase in friction. This was also noted by Ke and Wang (2007).

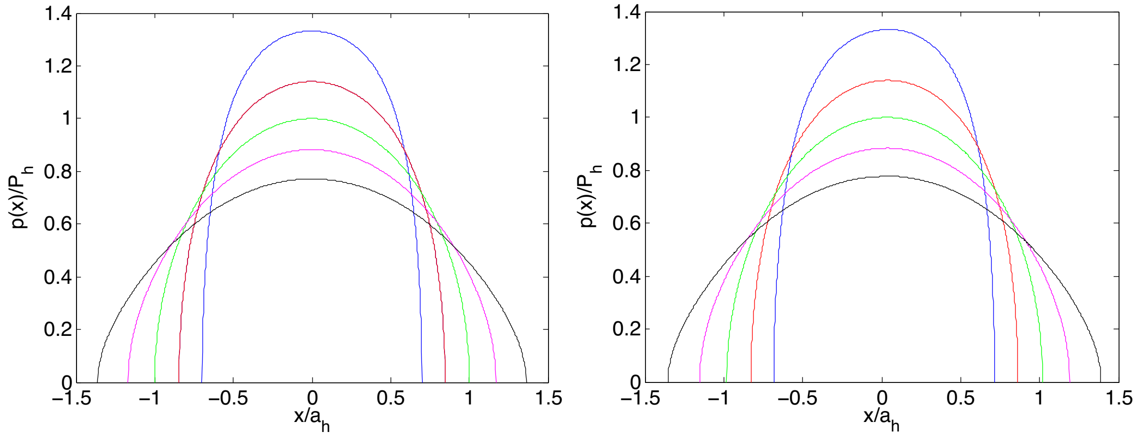

(a) $\eta = 0$

(b) $\eta = 0.1$

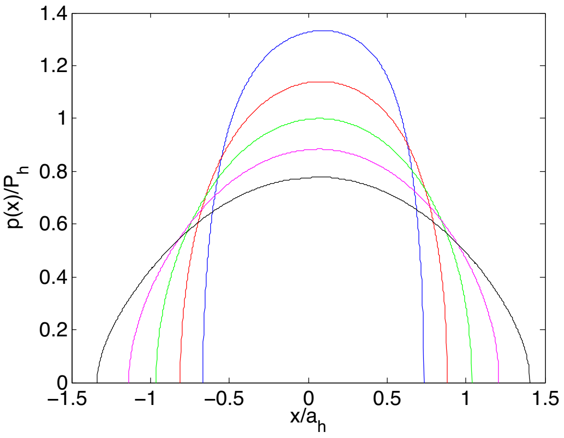

(c) $\eta = 0.2$

Figure 4: Plots of the predicted contact pressure curves produced for a selection of different coatings subject to three different values of friction. The blue line in this figure represents $\mu_1/\mu_0 = 4$, the red line $\mu_1/\mu_0 = 2$, the green line $\mu_1/\mu_0 = 1$, the magenta line $\mu_1/\mu_0 = 0.5$ and the black line $\mu_1/\mu_0 = 0.25$.

Another feature of interest in figure (5) is that the maximum contact pressure obtained for the hard coating increases as the interlayer thickness decreases whilst the maximum pressure for the soft coating decreases. This feature was observed by Chidlow and Teodorescu (2013) for the case of frictionless contact.

### 6.2. *Sub-surface stress fields*

We now wish to compute the sub-surface stress fields corresponding to the pressure curves produced in the previous section. The principal stresses that we use throughout this work are of Tresca type. This quantity is denoted $\tau_1$ and computed from the formula

$$\tau_1 = \sqrt{(\sigma_{xx} - \sigma_{yy})^2 + 4\sigma_{xy}^2}.$$

As the stresses within the solid are computed using the FFT, we need to determine an appropriate range of $x$ over which to evaluate the sub-surface stress field. This is equivalent to determining a suitable value of $L$ so that the interval $-L \leq x \leq L$ accurately captures the effects of the contact pressure.

Figure (6) presents the maximum principal stresses obtained using a range of values of $L$ for the coatings satisfying $\mu_1/\mu_0 = 0.5, 1, 2$ subject to the coating thickness $h_1/h_2 = 0.1$ and the friction coefficients given. We see in each case that the predicted maximum stress converges for $L/H \geq 10$ which is indicated by the lines flattening out. We therefore take $L = 10H$ within this work.

The sub-surface stresses depicted in figure (7) correspond to the pressure curves presented in figure (4) for the hard coating $\mu_1/\mu_0 = 2$ and the soft coating $\mu_1/\mu_0 = 0.5$ subject to the coating thickness $h_1/h_2 = 0.1$ and values of $\eta$ given. We see that the position of the maximum principal stress within the hard coating is transient and moves progressively closer to the solid surface as $\eta$

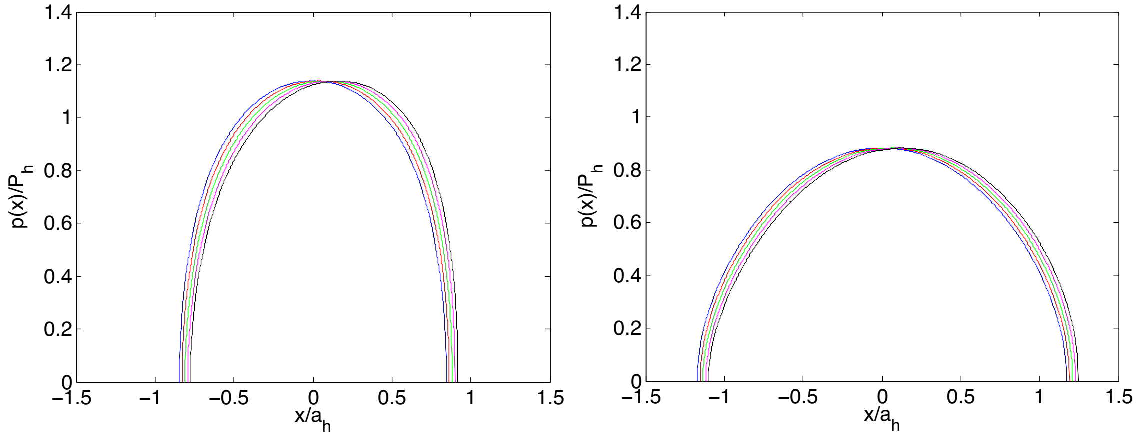

(a) $\frac{\mu_1}{\mu_0} = 2, \frac{h_1}{h_2} = 0.1$ (b) $\frac{\mu_1}{\mu_0} = 0.5, \frac{h_1}{h_2} = 0.1$

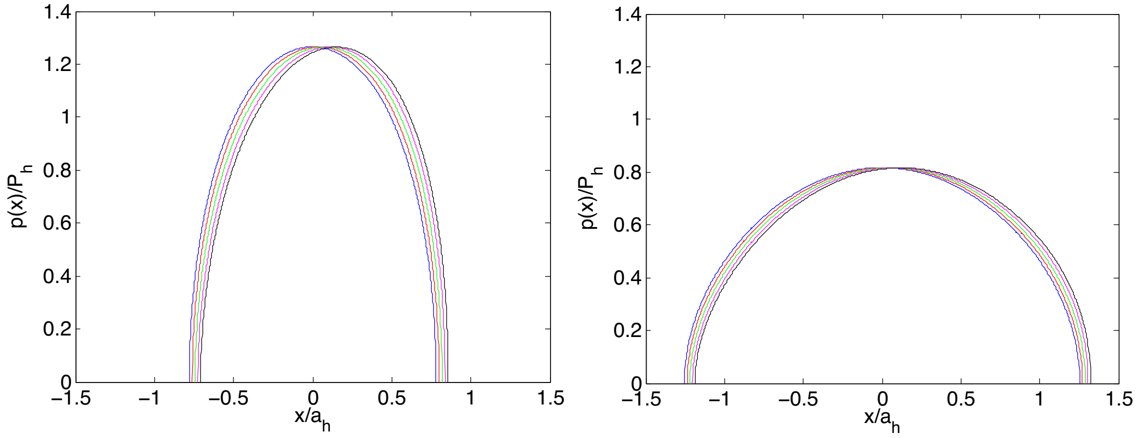

(c) $\frac{\mu_1}{\mu_0} = 2, \frac{h_1}{h_2} = 0.9$ (d) $\frac{\mu_1}{\mu_0} = 0.5, \frac{h_1}{h_2} = 0.9$

Figure 5: Plots of the predicted contact pressure curves produced for a hard and soft coating subject to two representative thicknesses and different values of the friction coefficient. Within this figure, the blue line represents $\eta = 0$, the red line $\eta = 0.1$, the green line $\eta = 0.2$, the magenta line $\eta = 0.3$ and the black line $\eta = 0.4$.

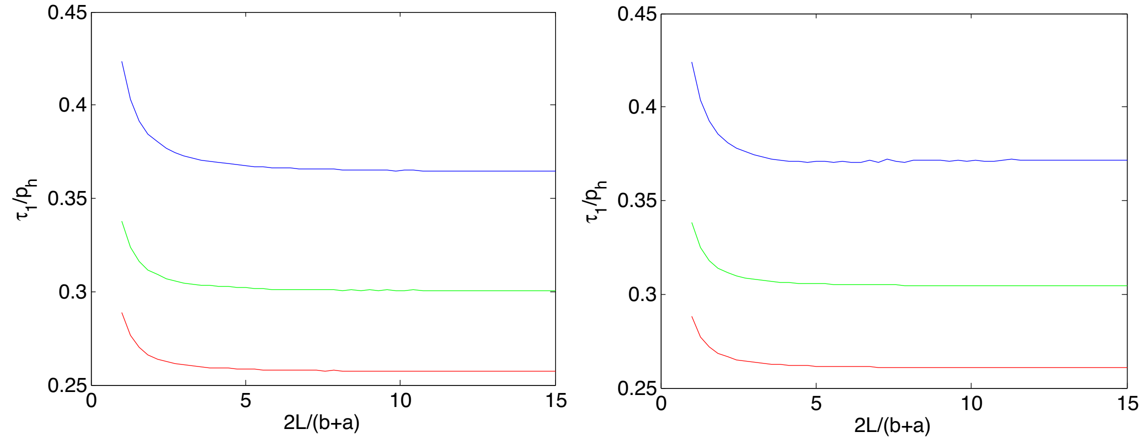

(a) $\eta = 0$ (b) $\eta = 0.1$

Figure 6: Plots of the maximum principal stress produced using the pressure curves in figure (4) against $L/H$ for three different coatings subject to two different values of $\eta$. The blue line represents $\mu_1\mu_0 = 2$, the green line $\mu_1/\mu_0 = 1$ and the red line $\mu_1/\mu_0 = 0.5$.

increases. The maximum value additionally occurs to the left of the origin for $\eta$ non-zero. This corresponds to the the maximum stress appearing in front of the punch as it slides over the surface.

The position of the maximum principal stress within the soft coating is also dependent on the friction coefficient $\eta$ but does not emulate the behaviour seen in the hard coating. In this situation, the location of the maximum stress does not move significantly as the friction increases but we do note the appearance of a region of high stress that occurs behind the punch as it slides. This is an interesting phenomenon as it indicates that the material puts up little resistance to the punch and thus will experience a large surface deflection in front of the punch in comparison to a hard coating.

The results presented in figure (8) depict the sub-surface stress fields produced for the same coatings subject to the coating/layer thickness ratio $h_1/h_2 = 0.9$ which corresponds to a thin inter-

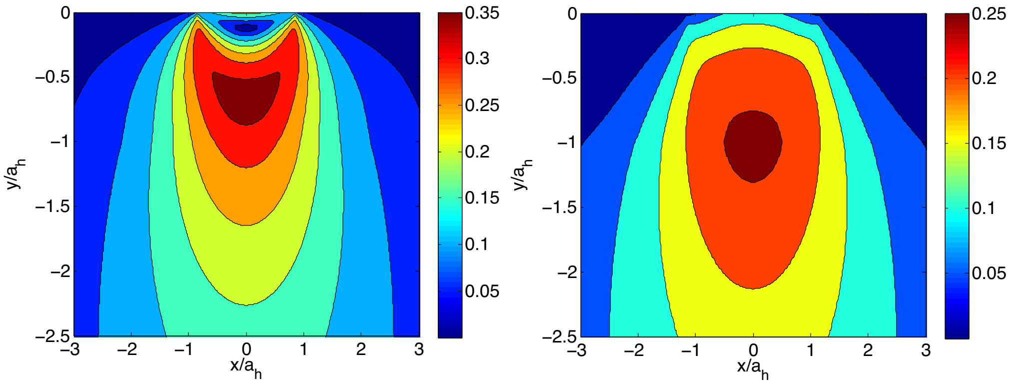

(a) $\frac{\mu_1}{\mu_0} = 2, \eta = 0$ (b) $\frac{\mu_1}{\mu_0} = 0.5, \eta = 0$

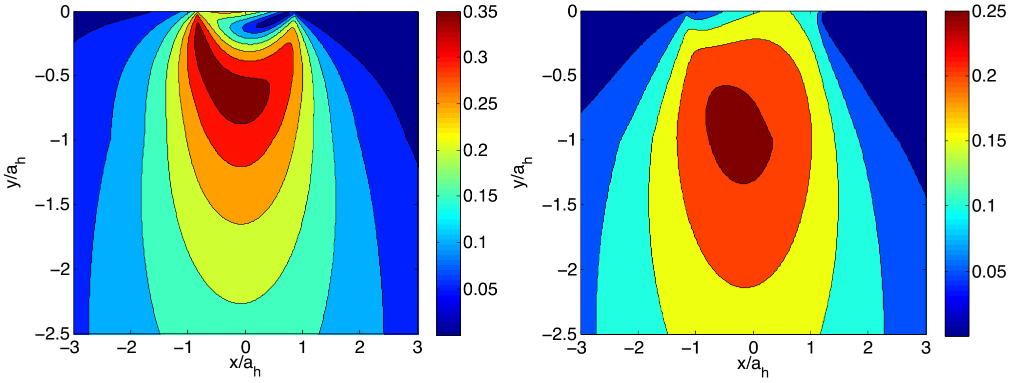

(c) $\frac{\mu_1}{\mu_0} = 2, \eta = 0.1$ (d) $\frac{\mu_1}{\mu_0} = 0.5, \eta = 0.1$

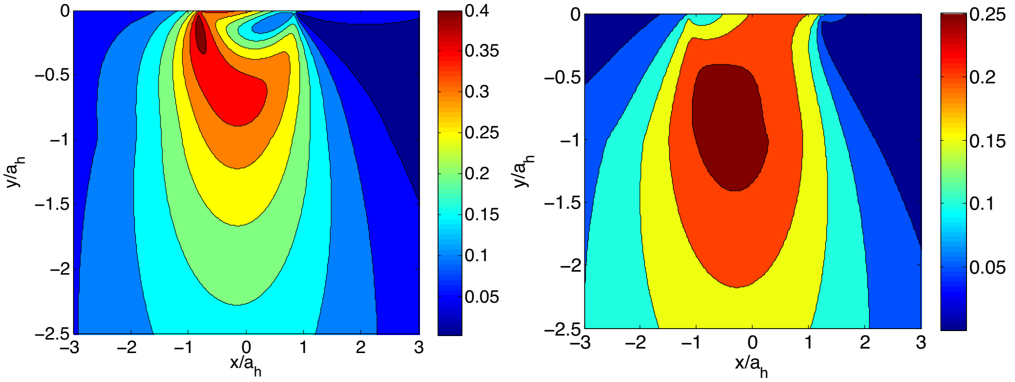

(e) $\frac{\mu_1}{\mu_0} = 2, \eta = 0.2$ (f) $\frac{\mu_1}{\mu_0} = 0.5, \eta = 0.2$

Figure 7: Plots of the sub-surface stress fields produced using the contact pressure curves in figure (4) for the hard coating $\mu_1/\mu_0 = 2$ and soft coating $\mu_1/\mu_0 = 0.5$ subject to the coating thickness $h_1/h_2 = 0.1$ and friction coefficients given.

layer. We see again here that the hard coating experiences a region of high stress close to its surface in front of the sliding punch whilst the soft coating experiences a region of high stress close to its surface behind the punch. It is observed in this example though that the position of the maximum principal stress does not change as $\eta$ varies in both coatings.

The magnitude of the maximum stress produced here for the hard coating is significantly higher than that given in figure (7). This seems to indicate that harder coatings attain their maximum stress when the transition layer is thin. The opposite seems to be true for the soft coating as its maximum principal stress seems to be attained when the coating is thin. It is however less conclusive where the maximum occurs for the case of a thin interlayer.

### *6.3. The effects of increasing friction within the contact*

The sub-surface stresses presented in section (6.2) indicate that the coating thickness and friction coefficient have a significant effect on the magnitude of the maximum principal stress. Our aim within this section is to determine the effects of the friction coefficient on the maximum principal stress that results from the contact problem. In order to do this, we consider how the maximum stress obtained within the layered solid subject to the four coatings satisfying $\mu_1/\mu_0 = 0.25, 0.5, 2, 3$ varies as the friction coefficient increases in magnitude. We take $0 \leq \eta \leq 0.3$ in this example and present results for the two representative coating thicknesses $h_1/h_2 = 0.1, 0.9$. As before we set $h_2/a_h = 1$. The notation

$$T = \max(\tau_1)$$

will be used in the following sections for simplicity.

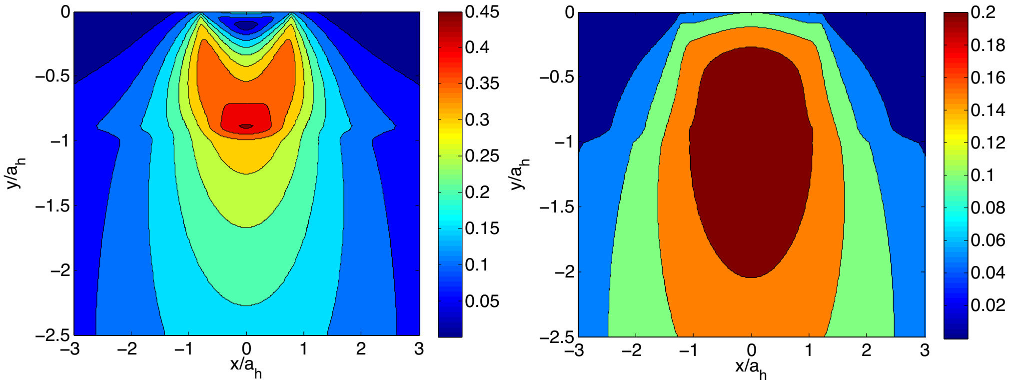

(a) $\frac{\mu_1}{\mu_0} = 2, \eta = 0$

(b) $\frac{\mu_1}{\mu_0} = 0.5, \eta = 0$

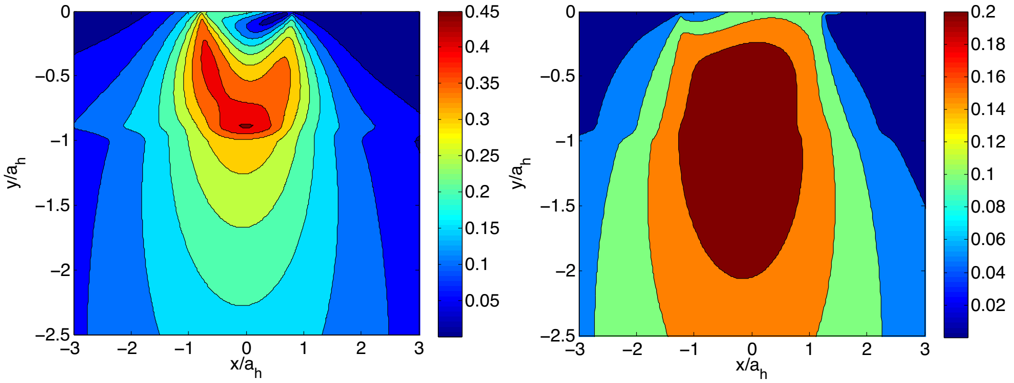

(c) $\frac{\mu_1}{\mu_0} = 2, \eta = 0.1$

(d) $\frac{\mu_1}{\mu_0} = 0.5, \eta = 0.1$

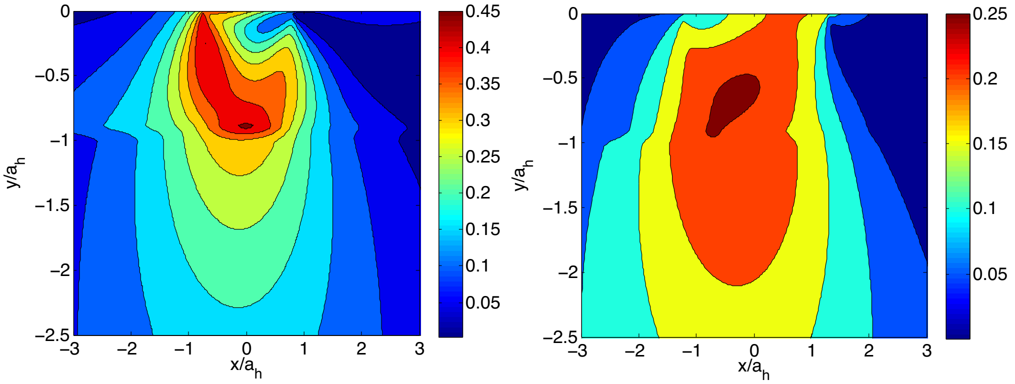

(e) $\frac{\mu_1}{\mu_0} = 2, \eta = 0.2$

(f) $\frac{\mu_1}{\mu_0} = 0.5, \eta = 0.2$

Figure 8: Plots of the sub-surface stress fields produced using the contact pressure curves in figure (4) for the hard coating $\mu_1/\mu_0 = 2$ and soft coating $\mu_1/\mu_0 = 0.5$ subject to the coating thickness $h_1/h_2 = 0.9$ and friction coefficients given.

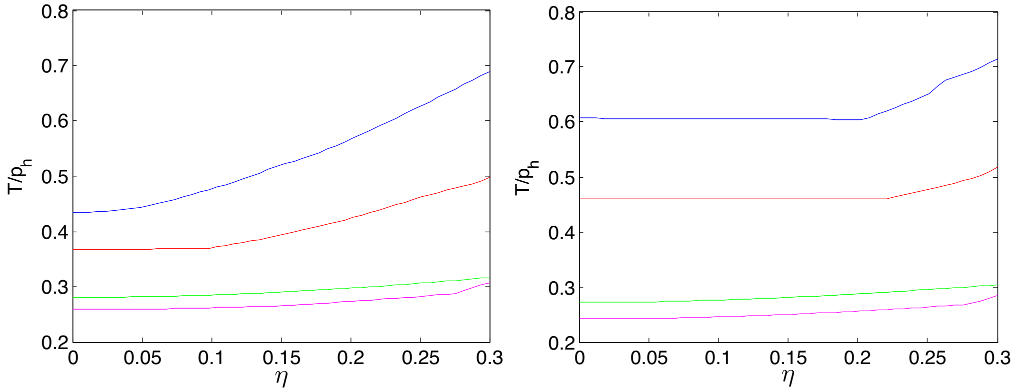

(a) $\frac{h_1}{h_2} = 0.1$ (b) $\frac{h_1}{h_2} = 0.9$

Figure 9: The effect of increasing friction on the dimensionless maximum principal stress $\tau_1/p_h$ for the coatings $\mu_1/\mu_0 = 3$ (blue line), $\mu_1/\mu_0 = 2$ (red line), $\mu_1/\mu_0 = 0.75$ (green line) and $\mu_1/\mu_0 = 0.5$ (magenta line).

Figure (9) depicts the results obtained for this problem. We can see that when $h_1/h_2 = 0.1$, the maximum stress obtained for each coating monotonically increases as $\eta$ increases. The increase in stress in the hard coatings is also much larger than that for the soft coatings with a maximum dimensionless stress of approximately 0.4 predicted for $\mu_1/\mu_0 = 3$ when $\eta = 0$ and 0.7 predicted when $\eta = 0.3$. Conversely, the soft coating $\mu_1/\mu_0 = 0.25$ experiences a maximum dimensionless stress of approximately 0.25 when $\eta = 0$ and 0.3 when $\eta = 0.3$. This indicates that hard coatings are more sensitive to the value of the friction coefficient.

The results presented for the case $h_1/h_2 = 0.9$ show that the maximum stress within the soft coatings monotonically increase with $\eta$ as before. However, this is not true for the hard coatings. The maximum stress within the hard coating $\mu_1/\mu_0 = 3$ remains constant until $\eta > 0.2$ and then begins to increase sharply. The stress within the hard coating $\mu_1/\mu_0 = 2$ remains constant for $\eta <\approx 0.22$ and then increases slowly. It is interesting to note here that the maximum stresses predicted for all four coatings are attained when $\eta = 0.3$ in both graphs and that these values are approximately the same despite the change in interlayer thickness. We conclude that whilst the maximum stress experienced for soft coatings is sensitive to the friction coefficient, the same is not necessarily true for hard coatings. Our results indicate that the ratio $h_1/h_2$ significantly alters the sensitivity of hard coatings to the friction coefficient.

### 6.4. *The effects of coating/interlayer thickness*

The results presented in the preceding sections suggest that the coating/interlayer thickness ratio $h_1/h_2$ is highly important in determining the magnitude of the maximum principal stress. We therefore conclude this work with an investigation into how the ratio $h_1/h_2$ effects the maximum principal stress that results from the contact problem.

Within this section, we plot $T/p_h$ against $h_1/h_2$ for the four different coatings $\mu_1/\mu_0 = 0.25, 0.5, 2, 3$ subject to the two different friction coefficients $\eta = 0.1, 0.2$ and dimensionless layer thicknesses $h_2/a_h = 0.5, 1$.

The results presented in figure (10) depict the dimensionless maximum stresses obtained for the stated parameter values. We can see here that the maximum principal stress experienced by the hard coatings in these examples generally increase as the ratio $h_1/h_2$ increases whilst the maximum stress within the soft coatings decrease. These observations are in accord with our results in section (6.2). We also note that the value of $T/p_h$ produced for each coating and different value of $h_1/h_2$ is relatively unaffected by the change in the total layer thickness $h_2/a_h$.

The most interesting feature of the graphs in figure (10) is that the maximum stress within the hard coatings sharply increases for certain values of $h_1/h_2$. This is particularly noticeable for the

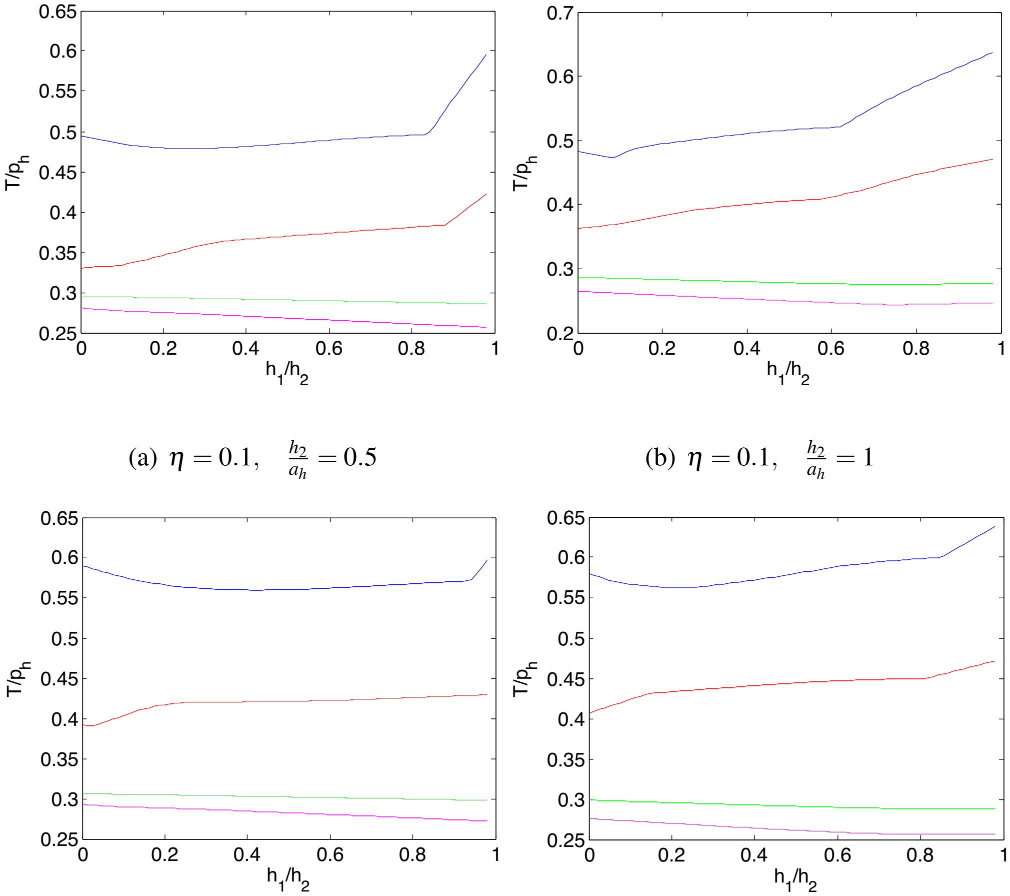

(a) $\eta = 0.1, \quad \frac{h_2}{a_h} = 0.5$

(b) $\eta = 0.1, \quad \frac{h_2}{a_h} = 1$

(c) $\eta = 0.2, \quad \frac{h_2}{a_h} = 0.5$

(d) $\eta = 0.2, \quad \frac{h_2}{a_h} = 1$

Figure 10: Plots of the dimensionless maximum principal stress against $h_1/h_2$ for four different coating types subject to the values of $\eta$ and $h_2/a_h$ given. The blue line represents $\mu_1/\mu_0 = 3$, the red line depicts $\mu_1/\mu_0 = 2$, the green line $\mu_1/\mu_0 = 0.75$ and the magenta line $\mu_1/\mu_0 = 0.5$.

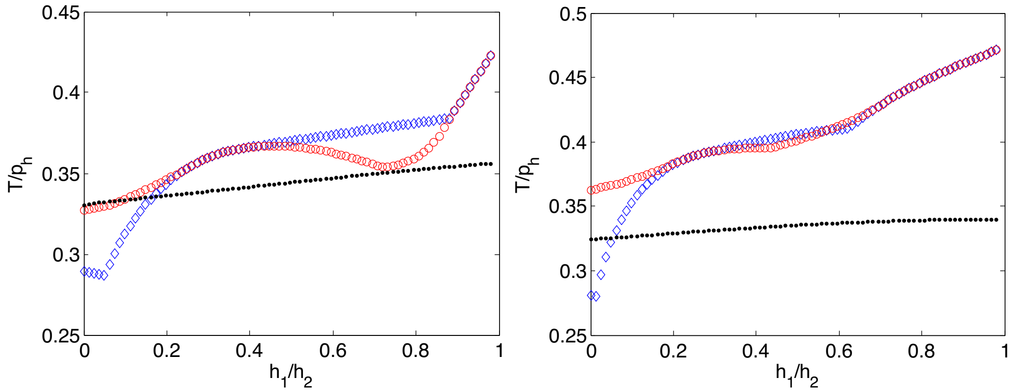

(a) $\eta = 0.1, \quad \frac{h_2}{a_h} = 0.5$

(b) $\eta = 0.1, \quad \frac{h_2}{a_h} = 1$

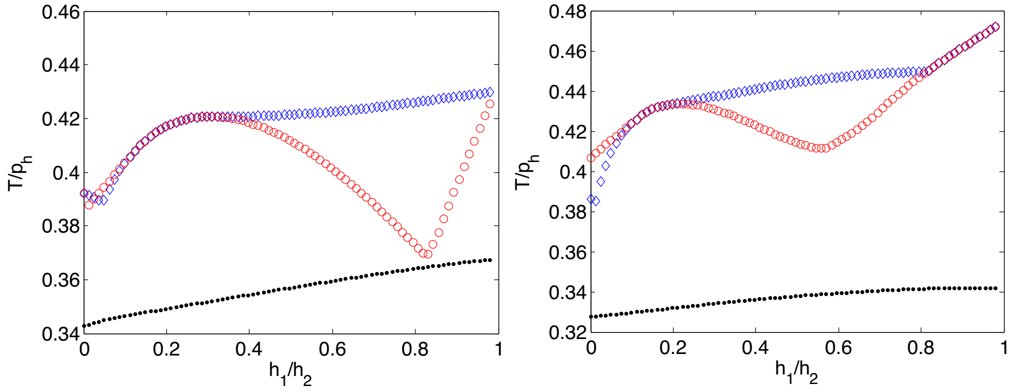

(c) $\eta = 0.2, \quad \frac{h_2}{a_h} = 0.5$

(d) $\eta = 0.2, \quad \frac{h_2}{a_h} = 1$

Figure 11: Plots of the maximum dimensionless prinicipal stress obtained within each region of the solid for the hard coating satisfying $\mu_1/\mu_0 = 2$ subject to the parameter values given. The blue diamonds represent the maximum stress within the coating, the red circles give the maximum stress within the interlayer and the black dotted line the maximum stress within the substrate.

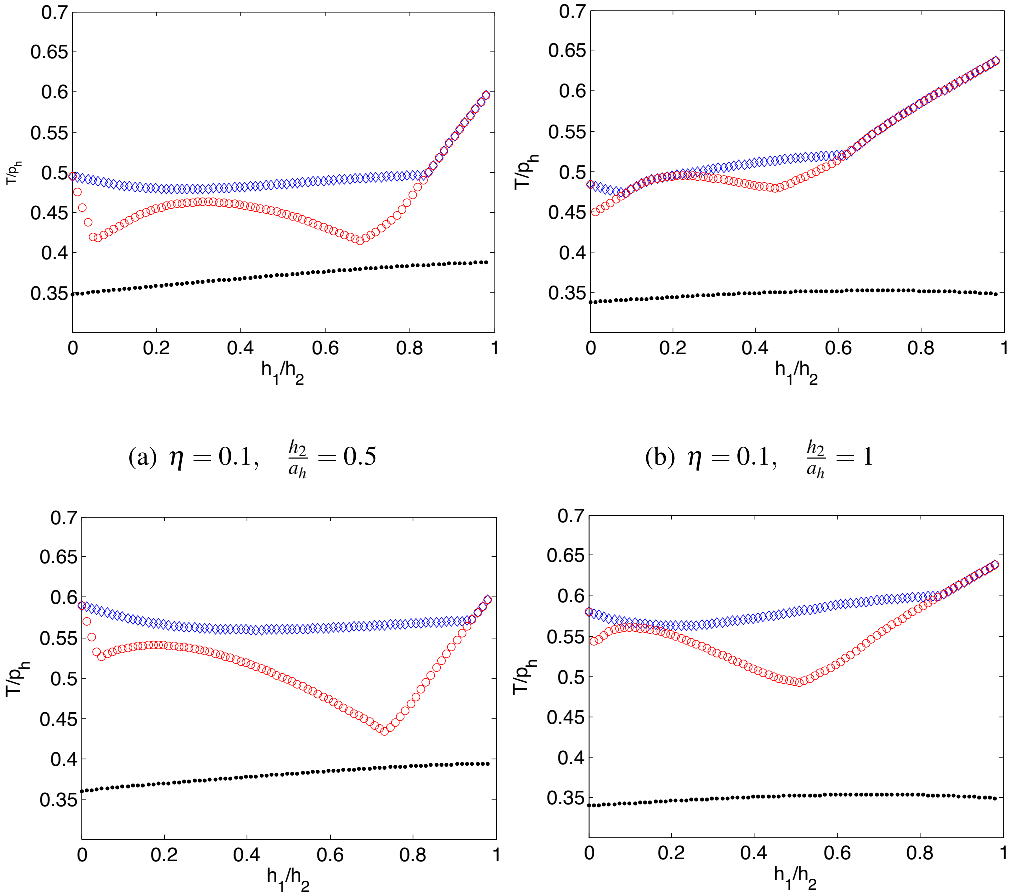

(a) $\eta = 0.1, \quad \frac{h_2}{a_h} = 0.5$ (b) $\eta = 0.1, \quad \frac{h_2}{a_h} = 1$

(c) $\eta = 0.2, \quad \frac{h_2}{a_h} = 0.5$ (d) $\eta = 0.2, \quad \frac{h_2}{a_h} = 1$

Figure 12: Plots of the maximum dimensionless prinicipal stress obtained within each region of the solid for the hard coating satisfying $\mu_1/\mu_0 = 3$ subject to the parameter values given. The key used here is the same as in figure (11).

harder coating $\mu_1/\mu_0 = 3$. In order to investigate what is causing this behaviour, we consider how the maximum principal stress within each region of the solid evolves as the ratio $h_1/h_2$ varies. We concentrate only on the hard coatings satisfying $\mu_1/\mu_0 = 2, 3$ and produce results for the parameter values given previously. These results are presented in figures (11) and (12).

We observe in both figures that the location at which the global maximum stress occurs is transient and depends on the ratio $h_1/h_2$. The local stresses within the coating and transition layer possess local maxima and minima for different values of $h_1/h_2$ whilst in both examples considered here the maximum stress within the substrate is monotonically increasing when $h_2/a_h = 0.5$ and relatively constant when $h_2/a_h = 1$.

By comparing the results in figures (11) and (12) with those in figure (10), we see that the sharp increases and decreases in the maximum stress observed before correspond to the location of the maximum stress changing between the transition layer and coating. For example, in figures (11a) and (12a), the sharp increase in the maximum stress at $h_1/h_2 = 0.9$ and $h_1/h_2 = 0.8$ respectively correspond to the maximum stress moving from the coating to the transition layer.

To emphasise the transient nature of the maximum principal stress, figure (13) depicts where the maximum principal stress occurs within the solid for the four different coatings already considered in this section. These results confirm our hypotheses from the previous figure and indicate that small changes in the coating thickness can result in the maximum principal stress occurring in different regions of the solid. They also suggest that the greater the thickness of the layer, the less likely the maximum stress is to occur in the substrate. This observation could potentially be very useful in coating design as thicker coatings can theoretically minimise the stress experienced by the base material and hence provide a greater degree of protection. The ratio $h_1/h_2$ would still need to be carefully controlled in this situation however as undesirably large stresses could still occur in the coating/transition region and could cause material failure.

## 7. Conclusions

We have presented a model that may be used to determine the stresses and displacements induced within a layered material comprising a coating- FGM layer- substrate through contact

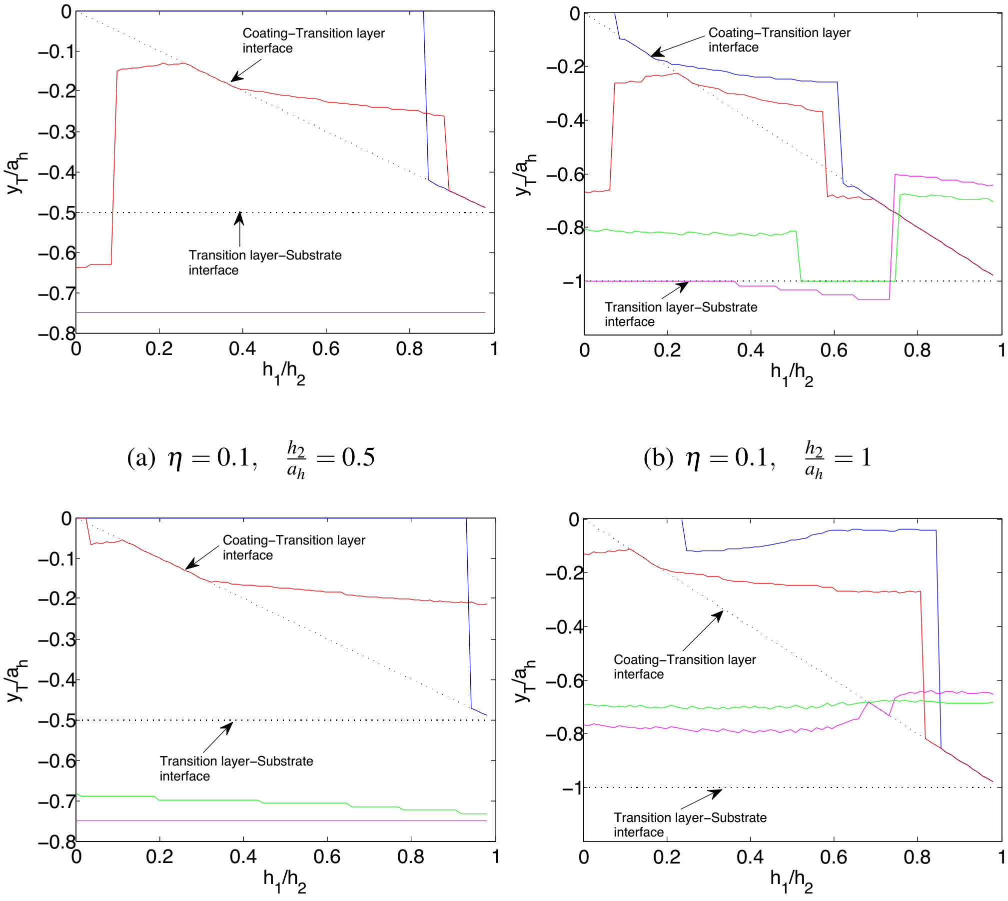

(a) $\eta = 0.1, \quad \frac{h_2}{a_h} = 0.5$

(b) $\eta = 0.1, \quad \frac{h_2}{a_h} = 1$

(c) $\eta = 0.2, \quad \frac{h_2}{a_h} = 0.5$

(d) $\eta = 0.2, \quad \frac{h_2}{a_h} = 1$

Figure 13: Plots of the dimensionless location at which the maximum principal stress occurs against $h_1/h_2$ for the results presented in figure (10). The blue line indicates the location of the maximum stress for the case $\mu_1/\mu_0 = 3$, the red line corresponds to $\mu_1/\mu_0 = 2$, the green line corresponds to $\mu_1/\mu_0 = 0.75$ and the magenta line $\mu_1/\mu_0 = 0.5$.

with another object. By initially considering the application of point forces to the layered solid at the origin, the stresses and displacements were computed in terms of the inverse Fourier transform and generalised to the case of normal and tangential tractions distributed over the solid surface using the superposition principle. A discussion of how to compute the stresses using the IFFT was also presented.

An integral equation was formulated for both the normal and tangential pressures applied to the solid surface and solved numerically for the case of contact with a rigid parabolic punch under the assumptions of Coulomb friction. The proposed model was then validated against literature accepted results in two different limiting cases.

The selection of numerical results produced for the full contact problem indicate that whilst increased friction within the contact makes little difference to the applied normal pressure, the resultant sub-surface stresses are greatly affected by the presence of friction. It was seen that the magnitude of the maximum principal stress was highly dependent on the hardness of the coating (ratio $\mu_1/\mu_0$), friction coefficient ($\eta$) and coating/interlayer thickness ratio ($h_1/h_2$). In particular, it was observed that hard coatings are particularly sensitive to the ratio $h_1/h_2$ as dramatic increases in the maximum attained stress and the location at which it occurs are observed as $h_1/h_2$ varies between 0 and 1. This sensitivity indicates that hard coatings need to be carefully tailored to ensure that they do not experience much larger stresses under pressure than expected.

## Appendix A. Contact model derivation

This section defines the matrices that appear in (19)-(23). Please note that all matrices are dependent only on the transform variable $\xi$.

$$K_j^{(i)} = \begin{pmatrix} e^{-\lambda_j h_i} & 0 \\ 0 & e^{-\lambda_{j+2} h_i} \end{pmatrix}, \tag{A.1}$$

$$N_j = \begin{pmatrix} 1 & 1 \\ \lambda_j & \lambda_{j+2} \end{pmatrix}, \tag{A.2}$$

$$M_j = \begin{pmatrix} \mathscr{F}(\lambda_j) & \mathscr{F}(\lambda_{j+2}) \\ \mathscr{G}(\lambda_j) & \mathscr{G}(\lambda_{j+2}) \end{pmatrix}, \tag{A.3}$$

$$H_j = \begin{pmatrix} 1 & -h_j \\ |\xi| & 1-|\xi|h_j \end{pmatrix}, \tag{A.4}$$

$$J_j = \begin{pmatrix} 1 & -h_j \\ -|\xi| & 1+|\xi|h_j \end{pmatrix}, \tag{A.5}$$

$$G_j = \begin{pmatrix} \xi^2 & 2(1-\nu)|\xi| - \xi^2 h_j \\ -|\xi|\xi^2 & \xi^2\Bigl((1-2\nu)+|\xi|h_j\Bigr) \end{pmatrix}, \tag{A.6}$$

$$L_j = \begin{pmatrix} \xi^2 & -\Bigl(2(1-\nu)|\xi| + \xi^2 h_j\Bigr) \\ |\xi|\xi^2 & \xi^2\Bigl((1-2\nu)-|\xi|h_j \end{pmatrix}, \tag{A.7}$$

$$\Phi = H_0 - e^{-2|\xi|h_1} J_0 \left(J_1 - SW^{-1}L_1\right)^{-1} \left(H_1 - SW^{-1}G_1\right), \tag{A.8}$$

$$S = N_1 K_1^{(1)} - N_2 K_2^{(1)} \left(T_2 K_2^{(2)}\right)^{-1} T_1 K_1^{(2)}, \tag{A.9}$$

$$W = M_1 K_1^{(1)} - M_2 K_2^{(1)} \left(T_2 K_2^{(2)}\right)^{-1} T_1 K_1^{(2)}, \tag{A.10}$$

$$T_j = N_j - H_2 G_2^{-1} M_j, \tag{A.11}$$

for $i, j = 1, 2$. The functions $\mathscr{F}$ and $\mathscr{G}$ appearing in (A.3) are further defined as

$$\mathscr{F}(\lambda_j) = (1-\nu)\lambda_j^2 + \nu\xi^2, \tag{A.12}$$

$$\mathscr{G}(\lambda_j) = (1-\nu)\lambda_j^3 - \alpha(1-\nu)\lambda_j^2 - \xi^2(2-\nu)\lambda_j - \alpha\nu\xi^2. \tag{A.13}$$

Please note that the notation $h_0 = 0$ has been adopted in this section.

## Acknowledgement

The authors acknowledge the technical support from partners and sponsorship provided by the EPSRC through the ENCYCLOPAEDIC program grant

## References

Çömez, I., Erdöl, R., 2012. Frictional contact problem of a rigid stamp and an elastic layer bonded to a homogeneous substrate. Archive of Applied Mechanics , DOI 10.1007/s00419–012–0626–4.

Chidlow, S.J., Teodorescu, M., 2013. Two-dimensional contact mechanics problems involving inhomogeneously elastic solids split into three distinct layers. International Journal of Engineering Science 70, 102–123.

Choi, H.J., 2012. Interaction of two offset interfacial cracks in bonded dissimilar media with a functionally graded interlayer. Mechanics Research Communications 45, 7–14.

Guler, M.A., Erdogan, F., 2004. Contact mechanics of graded coatings. Int. J. Solids Structures 41, 3865–3889.

Guler, M.A., Erdogan, F., 2007. The frictional sliding contact problems of rigid parabolic and cylindrical stamps on graded coatings. Int. J. Mech. Sciences 49, 161–182.

Johnson, K.L., 1985. Contact Mechanics. Cambridge University Press, Cambridge.

Ke, L.L., Wang, Y.S., 2006. Two-dimensional contact mechanics of functionally graded materials with arbitrary spatial variations of material properties. Int. J. Solids Structures 43, 5779–5798.

Ke, L.L., Wang, Y.S., 2007. Two-dimensional sliding frictional contact of functionally graded materials. European Journal of Mechanics A/Solids 26, 171–188.

King, R.B., O'Sullivan, T.C., 1987. Sliding contact stresses in a two-dimensional layered elastic half space. Int. J. Solids Structures 23, 581–597.

Ma, L.F., Korsunsky, A.M., 2004. Fundamental formulation for frictional contact problems of coated systems. Int. J. Solids and Structures 41, 2837–2854.

Suresh, S., 2001. Graded materials for resistance to contact deformation and damage. Science 292, 2447–2451.

Suresh, S., Olsson, M., Giannakopoulos, A.E., Padture, N.P., Jitcharoen, J., 1999. Engineering the resistance to sliding-contact damage through controlled gradients in elastic properties at contact surfaces. Acta mater. 47, 3915–3926.

Teixeira, V., 2001. Numerical analysis of the influence of coating porosity and substrate elastic properties on the residual stresses in high temperature graded coatings. Surface and Coatings Technology 146-147, 79–84.

Teodorescu, M., Rahnejat, H., Gohar, R., Dowson, D., 2009. Harmonic decomposition analysis of contact mechanics of bonded layered elastic solids. Applied Mathematical Modelling 33, 467–485.

Timoshenko, S.P., Goodier, J.N., 1970. Theory of Elasticity. McGraw-Hill, Singapore.

Yang, J., Ke, L.L., 2008. Two-dimensional contact problem for a coating-graded layer-substrate structure under a rigid cylindrical punch. International Journal of Mechanical Sciences 50, 985–994.